necessary to maintain the wheels spinning at the initial rate. The traces of the eigenvector components in Fig. 6 show that the initial stored momentum causes the eigenvector orientation to vary during the slew as predicted by the theory. However, this variation is not excessive and does not introduce any instabilities into the control system. The curves in Fig. 6 show that the system performance does not greatly deteriorate when operating with initial angular momentum.

Concluding Remarks

The test results shown in Figs. 4–6 show that the wide angle attitude control system based on Euler's theorem on rotation performs as predicted by the theoretical analysis. The test results indicate that the system can stabilize the body with a high degree of accuracy at the target position. It was also shown that a redundant type of control system package could be implemented which would avoid a flight abort in case of gyroscope failure.

The type of control system shown in this mechanization could be used very effectively on a vehicle such as the OAO where it is desired to command the spacecraft through large angles. The system has proven global stability and the path it will take during a slew is well-behaved and predictable. It also results in a direct motion about a single axis rather than about three axes separately which may make it a desirable type of control for a manned vehicle.

References

[1] Meyer, G., "On the Use of Euler's Theorem on Rotations for the Synthesis of Attitude Control Systems," TN D-3643, 1966, NASA.

[2] Goldstein, H., *Classical Mechanics*, Addison-Wesley, Reading, Mass., 1959.

JULY 1970 J. SPACECRAFT VOL. 7, NO. 7

Strapdown Inertial Attitude-Indication Evaluations

JEROLD P. GILMORE* AND RICHARD A. MCKERN†
Charles Stark Draper Laboratory, Massachusetts Institute of Technology, Cambridge, Mass.

Results of a test-evaluation study of the strapdown mechanization for inertial-grade attitude indication are presented. An experimental gyro test package, dynamic test facility and computational attitude algorithm are described. Static and dynamic test results obtained using real-time monitoring are presented with error propagation profiles. Single-degree-of-freedom gyros were mechanized in a digital torque-to-balance control loop. The gyro incremental output data were processed in real-time in a digital computer to correct for instrument error sources and perform the attitude transformation update. Whole-number quaternion algorithms were developed and performance trade offs for various algorithm parameters are presented with confirming test results. The bounds of realizable system performance are shown to be dependent on instrument parameter stability and algorithm bandwidth. Performance in various application environments may be projected by the results presented.

Introduction

UNLIKE other studies[1,2] this program employed integrated real-time system test evaluations to explore the inertial-attitude indication capabilities of the pulse-torque-to-balance gyro strapdown configuration. Thus, a structure-mounted gyrotest package, a dynamic test table, torquing electronics and associated power supplies, and a computational facility were assembled. Similarly, studies on instrument error sources and attitude reference algorithms were conducted and synthesized into operating software. Static and dynamic tests were then devised and conducted with an aim towards determining hardware-software tradeoff performance criteria and limitations.

System Test Configuration

Test Package

The experimental test package shown in Fig. 1 contains three orthogonally mounted 18-size Inertial Reference Integrating Gyroscopes (18IRIG). Each gyro is mounted in an alignment fixture and normalized with a signal-generator preamplifier, suspension and quadrature networks and a temperature controller. An optical cube mounted on the frame is the alignment reference, allowing determination of the test package orientation relative to azimuth and local-vertical. The frame is aluminum with coolant passages for air-to-liquid heat exchanger operation and is shrouded for environment isolation. Three sets of pads form a triad of planes that mate with the gyro alignment fixture. This fixture allows independent adjustment of the gyro input axis (IA) about its spin axis (SA) and its output axis (OA). The package form factor allows for substitution within the gimbals of an Apollo Inertial Measurement Unit for special dynamic testing. In this evaluation the package was mounted on the precision 4 axis test table via a high-thermal resistance, adjustable alignment plate. Test-table positioning accuracy is calibrated to 2 arc sec. Constant rates of up to 1 rad/sec and oscillatory frequencies of up to 10 Hz can be obtained about two of its rotary axes. Thus, precision static orientation, rate, and oscillatory input capabilities allowed gyro drift parameter, scale-factor, and end-to-end dynamic performance test determinations. The test configuration, the computer, and the dynamic test table on which the experimental test package is mounted are shown in Fig. 2.

Presented as Paper 69–849 at the AIAA Guidance Control, and Flight Mechanics Conference, Princeton, N. J., August 18–20, 1969; submitted August 27, 1969; revision received February 11, 1970. Conducted at the Massachusetts Institute of Technology, Charles Stark Draper Laboratory under the auspices of the NASA Manned Space Flight Center, Contract NAS 9-6823.

* Director, Apollo Inertial Subsystems.
† Assistant Director, Systems Analysis.

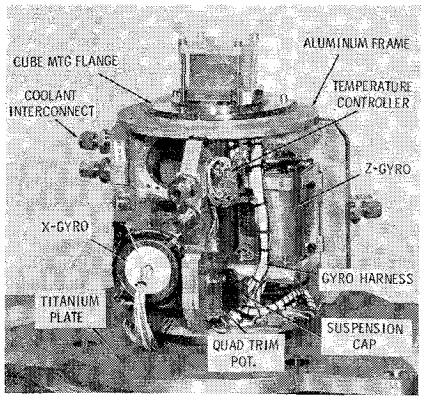

Fig. 1 Gyro test package X and Z gyro view.

The 18 IRIG MOD B[3,4] is a floated single-degree-of-freedom state-of-the-art gyroscope under development at the Charles Stark Draper Lab. Designed for strapdown application, it incorporates a permanent-magnet torquer for torque-to-balance operation with input rates of up to 1 rad/sec and magnetic suspension, preventing radial side loading for rates in excess of 1 rad/sec. A gas bearing wheel package is used for extended operational life. (Ball-bearing degradation has accounted for 50% of Apollo gyro performance rejections.) The 18-IRIGs used were developmental instruments and, because of this evaluation, design refinements have been incorporated, i.e., increased torquer scale factor sensitivity and improved linearity, reduced signal-generator noise, etc.[5] These improvements are currently being phased into a second-development build. Table 1 lists some of the nominal design parameters of the 18 IRIGs used in this test program.

Torque Electronics

The instrument was operated in a ternary pulse-torque-to-balance control loop. A block diagram of the control loop is depicted in Fig. 3. The control loop applies a restraining torque via the gyro torque generator (TG) to maintain the gyro output axis at a null position. Output from the loop consists of torque pulses that represent quanta of rotation about the gyro input axes. These increments, processed through computer attitude-maintenance algorithms, provide a body-axis representation of the package attitude with respect to an inertial coordinate frame.

The control loop, on the basis of the gyro signal generator (SG) output (a 9600-Hz sine wave, whose amplitude and phase are proportional to the magnitude and direction of the gyro float angle displacement from null), applies current pulses of fixed amplitude and width, to the TG, via the interrogator (threshold detection and sampling logic) and current switch.

Torque current commands are issued when the SG signal exceeds a threshold level at interrogation (4800-pps sampling

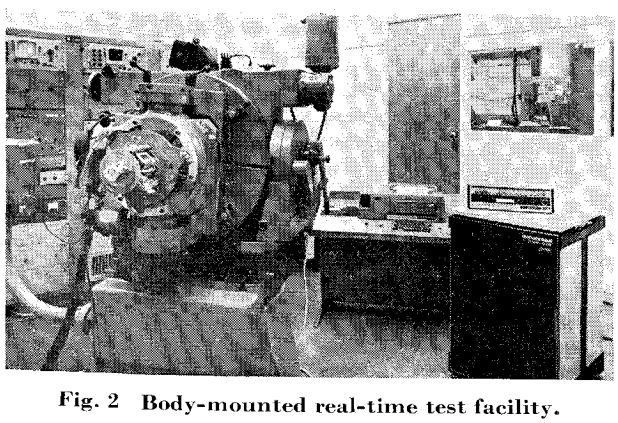

Fig. 2 Body-mounted real-time test facility.

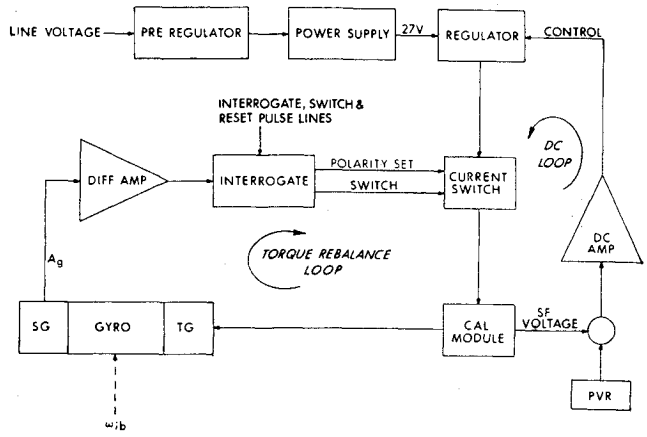

Fig. 3 Block diagram, ternary pulse torque electronics.

phased to the peak of the 9600-Hz SG signal). Timing pulses (switch and reset) operate through the logic to apply the current as a fixed period pulse. The ratio of the current period to the interrogation period is referred to as the torque-current duty cycle. The current amplitude is precisely maintained by a regulating d.c. control loop that operates on a voltage differential between the calibration-module resistor and a precision-voltage reference (PVR).

In summary, the torquing loop operates such that current applied as pulses develops a restraining torque proportional to a pulse rate at each input rate to the gyro. Each torque pulse represents an increment of equivalent input-angle rotation. Basic torque-loop parameters used during testing are listed in Table 2.

These parameters are typical of what may be anticipated in actual system application. The dependence of strapdown system performance on torque loop stability is illustrated by the relative sensitivity of the gyro torquer scale factor (SF) to variations in current and pulse width, (one part per million for a 70-nA current or a 0.1-nsec pulse-width change). Gyro-loop drift performance stability is also a significant application factor, thereby making essential the evaluation of both SF and drift stabilities in a system configuration over an extended operational period with moding, random environment changes, and repeated test sequencing. Test results are presented in later sections of this paper.

Computational Facility

The real-time algorithm computation was accomplished in a Honeywell DDP-516 computer, that interfaced with the gyro-package data counters and an 18-bit encoder (5 arc sec resolution) mounted to the rotary axis of the test table. A general purpose computer allowed flexible evaluaton of various whole-number attitude-maintenance mechanizations (direction-cosine matrix and the quaternion) and algorithm

Table 1 Nominal parameters, 18 IRIG MOD B 410 series

Angular momentum, H	0.151×10^6 gm-cm²/sec
Output axis damping coefficient, C_{OA}	675,000 dyne-cm-sec
Output axis inertia, I_{OA}	225 gm-cm²
Float time constant, $t_f = I_{OA}/C_{OA}$	333 μsec
Transfer function, $S_{SG}H/C_{OA}$	4.4 mv/mrad
Torquer scale factor, S_{tg}	775 dyne-cm/mA
Torquer time constant, $t_{tg} = L/R$	55 μsec
Anisoinertia coefficients, $(I_{SA} - I_{IA})/H$	9.2 deg/hr/(rad/sec)²
Wheel speed	24,000 rpm
Motor excitation	28v, 800Hz, 5.2 w

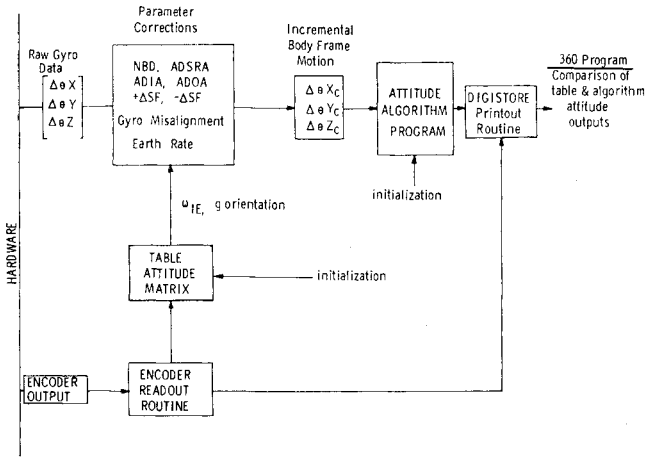

Fig. 4 System software mechanization.

parameters (expansion order, update frequency, and word length). Software was developed to allow management of peripheral input-out devices and processing under interrupt by priority-type controls. An interleaving capability was incorporated for recording the system data on the digistore (a high-speed incremental recorder) for fine grain evaluation.

The DDP-516 computer was used, since its speed (0.96-μsec memory cycle time), instruction complement, and interrupt structure were well suited for the attitude-maintenance algorithm application. In the memory, the algorithm, parameter correction, and input-output programs use 1500 words, and the executive program uses another 1500 words. The algorithm updating rate is 100/sec, parameter correction rates are 5–25/sec, and the attitude transformation output data rate is 6/sec. This complete mechanization with a third-order algorithm required 40% of available machine time; a first-order algorithm reduced the load by 12%.

Instrument Package Errors

System operation requires correction of gyro drift parameters, misalignments, and SF deviation. Accurate calibration and the stability of these parameters are a determining factor in the system performance. Static drift terms are both the nonacceleration sensitive bias (NBD) and the acceleration (g) sensitive biases defined by the SDF gyro axes (i.e., ADIA, ADSRA, ADOA). Gyro misalignments, expressed as two angular components (e.g., the Z-gyro misalignments are γ_{ZX} and γ_{ZY}), are defined with respect to the optical reference-cube axes and represent each gyro's IA misalignment with respect to the reference-cube normal.

The gyro SF corresponds to the angular scaling of each gyro $\Delta\theta$ pulse (Table 2). In practice, SF is adjusted to within a few hundred parts per million of a nominal scaling of 2^{-15} rad/pulse, and SF deviation is accurately calibrated as a base-line parameter. In the actual gyro, individual positive and negative SF weighting may be exhibited and must be separately calibrated. Similarly, SF weighting may deviate as a function of input rate.

These parameters were corrected by software in the system mechanization, Fig. 4. For example, for g-sensitive parameters, package orientation with respect to local vertical is computed in real time using the test-table position and rotational axis-encoder information, the g vector is resolved along the appropriate gyro sensitive axes, resultant drifts are calculated, and the observed raw gyro data are corrected. Thus, errors propagated in static performance are a function of correction parameter stability.

Table 2 Basic torque-loop parameters

Threshold detection and $\Delta\theta$ quantization	2^{-15} rad, 6.3 arc sec
Interrogation rate	4800 pps
Duty cycle	150/360 (86 μsec)
Torquer current	73 ma

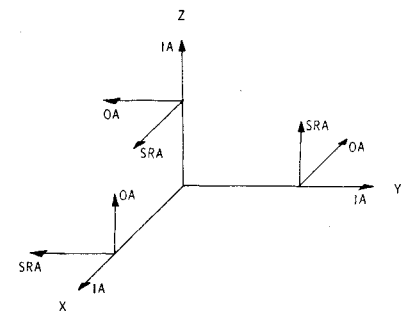

Fig. 5 Orientation of axes for gyro test package.

Instrument orientations relative to the test-package primary triad are shown in Fig. 5. Since the system is orthogonal, error-propagation characteristics are symmetrically evidenced on all axes. The DDP-516 was used to evaluate each of the static parameters, e.g., a 6-position orientation test relative to local vertical and azimuth allowed calibration of all drift parameters; rotational inputs about three positions provided SF and misalignment calibrations.

Y axis drift data (in meru) typify long-term drift magnitudes obtained from the 6-position calibration test (Fig. 6). A meru corresponds to 1/1000 of Earth's rotational rate (approximately 0.015°/hr). Such torque-to-balance data are consistent with long term gyro performance trends using standard gyro test-table servoed data. Corresponding long term scale factor magnitude characteristics evidenced on the Y system gyro for a fixed 5.7°/sec rate are shown in Fig. 7. Note the distinct difference in the plus-to-minus scale factor. The Y-gyro scale factor deviation vs input rate, corresponding to the scale factor measurements, is also shown in Fig. 8. Across the input test range, maximum excursions in linearity are on the order of 50 ppm. These data were typical of performance across many system cooldowns, varying test environment, and wheel start-stop sequences. On the average, 3500 wheel hr and 100 wheel stop-starts were accumulated on each gyro.

For high performance attitude indication the long term drift performance obtained shows that periodic calibration is required in much the same fashion as in existing gimbal systems. Shifts observed in the SF calibrations are believed to be induced by the effect on the bread-board torque-electronic loops of a test laboratory thermal shift in excess of 4°C (air conditioning outage). This illustrates the importance of maintaining the electronics at a stable temperature. Short-term continuous-operation gyro drift performance has been significantly better than the long term trend data, e.g.,

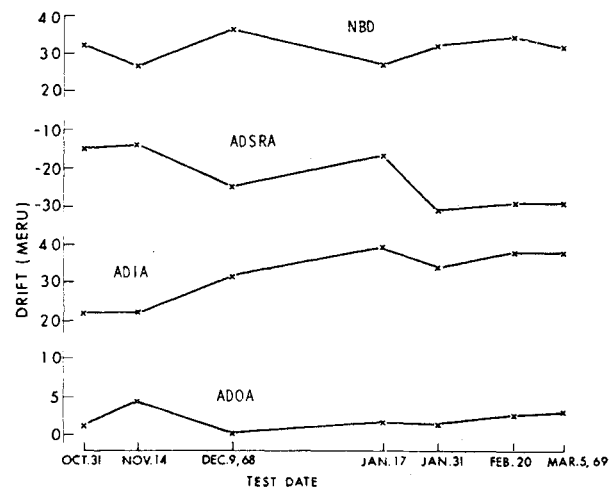

Fig. 6 Gyro drift Y-system gyro, 18 IRIG No. 413.

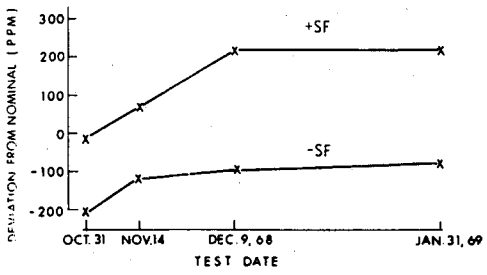

Fig. 7 Gyro SF long term performance for Y-system gyro, 18 IRIG No. 413.

Fig. 13 illustrates typical short term system performance in which better than 1-meru static drift stability was maintained.

In addition to the static terms there are dynamic error sources associated with the use of the SDF gyroscope in a strapdown environment. The major sources applicable to our tests were: output axis coupling, cross coupling, and anisoinertia. The simplified error equations corresponding to these and expressed in terms of an equivalent input-axis rate error (W_D) are

$$W_{DOA} = \dot{W}_{OA} I_{OA}/H \quad \text{output-axis coupling} \quad (1)$$

$$W_{DSA} = A_{cf} W_{SA} \quad \text{cross-coupling} \quad (2)$$

$$W_{DI} = (W_{SA} W_{IA})(I_{SA} - I_{IA})/H \quad \text{anisoinertia} \quad (3)$$

where $\dot{W}_{OA}$ = angular acceleration about the gyro output axis, W_{SA} = angular rate about the gyro spin axis, $I_{(\,)}$ = float inertia about the input, output or spin axes, H = wheel angular momentum, and A_{cf} = float rotational angle from its null OA position.

Equations (1) and (3) can be evaluated using the gyro parameters in Table 1 and corrected in the system software. The cross coupling error is a function of the torque-loop threshold and quantization. In the pulse-rebalance mechanization used for these tests the cross coupling error effect was negligible. In slew and oscillatory testing, the direct influence of these parameters is in evidence.

Algorithms

The attitude algorithm function in Fig. 4 computationally derives test-package attitude with respect to inertial space by operating on the corrected body-frame rates. Whole number computational techniques were used and various algorithms (quaternion and direction cosine) were studied. In this testing, results using the quaternion of rotation are described.[6]

The quaternion is a four-parameter representation of a body frame rotation with respect to an inertial-reference frame. Visualize a rotation by some angle θ of the body frame with respect to the inertial frame about a rotational axis $1_n{}^b$. The unit quaternion describing this rotation is defined as

$$q = \cos\theta/2 + \bar{1}_n{}^b \sin\theta/2 = \lambda + \bar{p}_x + \bar{p}_y + \bar{p}_z \quad (4)$$

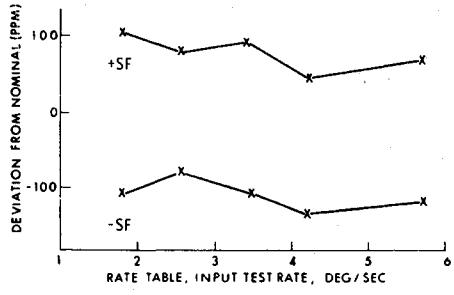

Fig. 8 Gyro SF; variation with rate Y-system gyro, 18 IRIG No. 413.

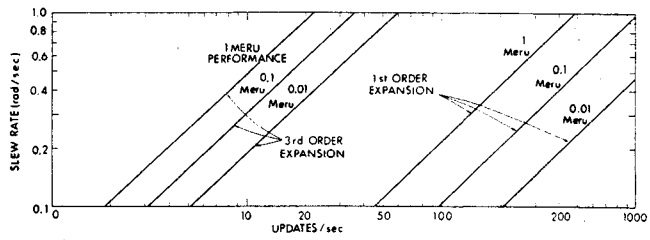

Fig. 9 Algorithm tradeoff constant slew environment.

This representation has no singularities and a single constraint

$$(\cos\theta/2)^2 + (\sin\theta/2)^2 = 1 \quad (5)$$

The algorithm yields a continuously updated quaternion-attitude representation by operating on body-rate data via the relationship

$$\dot{q} = q\Omega, \quad \Omega = (0 + \bar{W}^b/2) \quad (6)$$

($\bar{W}^b$) is the body rate expressed in body-frame coordinates. Since both the data and processing are digital, the solution is developed using Taylor series expansions for both the quaternion attitude and the incremental gyro information. Both the first- and third-order expansions were evaluated for slew, bandwidth, and round-off error propagation.

(Although the quaternion algorithm exhibits no significant error minimization advantages over an equivalent direction-cosine expansion, its single-length constraint, Eq. (5), rather than the direction-cosine orthogonalization constraint, simplifies processing and, since only four elements are outputed, allows higher digistore recording rates.)

Constant-Rate (Slew) Performance

The normalized error (E) per quaternion update for 1st, 2nd, and 3rd order expansions are, respectively,

$$E_1 = |(W^b \Delta T/12)|^3; \quad E_2 = \tfrac{1}{2}E_1$$
$$E_3 = |(W^b \Delta T/480)|^5 \quad (7)$$

where ΔT is the time between updates.

Relative performance tradeoffs between computational update rates and expansion order for various slews are illustrated in Fig. 9; e.g., to achieve 0.1-meru performance in a system sized for 0.5 rad/sec slew the first- and third-order expansions require 500 and 17 updates/sec respectively.

Coning Bandwidth

Coning,[6] a kinematic drift, occurs in a SDF gyro mechanization when identical-frequency phase-displaced sinusoids

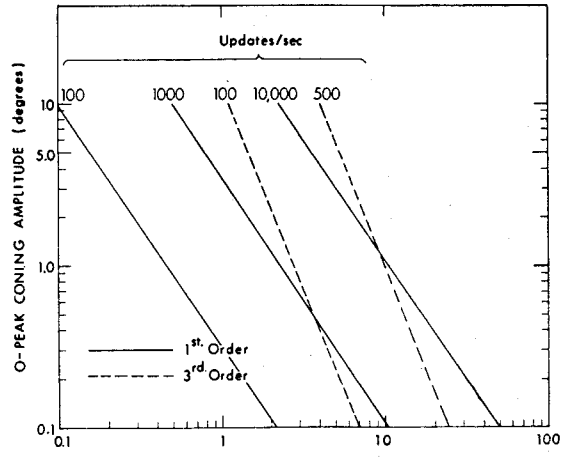

Fig. 10 Algorithm tradeoff showing 1-meru performance in a coning environment.

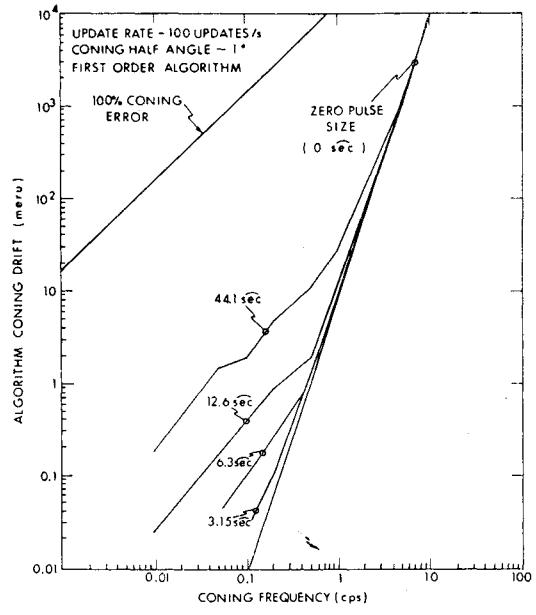

Fig. 11 Worst-case quantization effects in a coning environment.

are simultaneously applied about two orthogonal system axes. The gyro along the third axis then has an output corresponding to

$$W_b = (AB \sin\delta)\omega/2 \tag{8}$$

where A and B are the 0-to-peak amplitudes of the input sinusoid, δ is the relative phase displacement between them, and ω the input frequency.

Algorithms were developed that recognize and account for the coning environment. Range and performance are dependent upon the algorithm response characteristics. Figure 10 illustrates range and performance for first- and third-order expansions at comparative computational rates, i.e., better than one-meru drift correction is achieved for coning amplitudes and frequencies to the left of each line. The results illustrated are applicable to both quaternion and direction-cosine algorithms using infinite gyro $\Delta\theta$ resolution. Although performance deteriorates with $\Delta\theta$ quantization, degradation was not significant for a $\Delta\theta$ quantization of 6.3 arc sec in the tests conducted (Fig. 11).

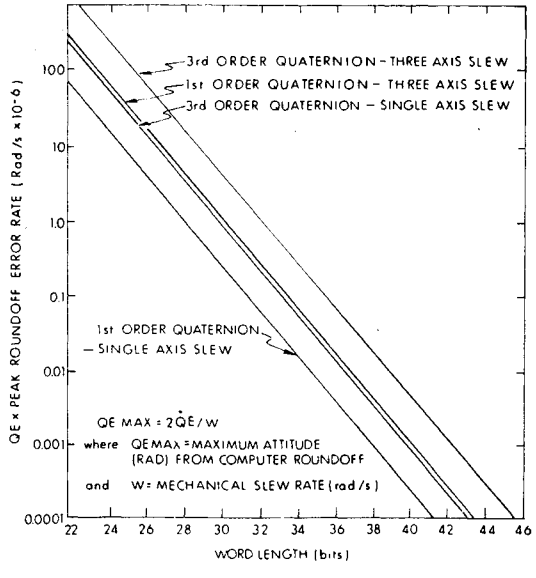

Fig. 12 Computer roundoff error vs wordlength.

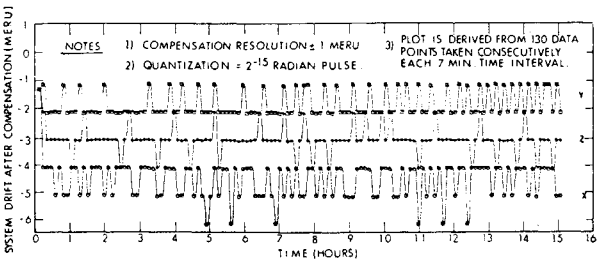

Fig. 13 System test results—Earth rate input.

Roundoff-Error Propagation

Algorithm error propagation caused by computational roundoff was evaluated and performance tradeoffs relating wordlength to performance for a slew environment are illustrated in Fig. 12. The quaternion attitude error propagated is sinusoidal at a frequency of one-half the mechanical slew rate, $|W|$, although the magnitude of the real-time roundoff error propagation is itself not dependent on slew rate. The peak magnitude of the error is dependent upon computational word length, algorithm arithmetic operations, and update rate. The figure is a normalized presentation in which the peak roundoff drift rate error ($\dot{Q}_E$) is plotted against computer word length for operations at 100 updates per second and is applicable only for slew rates in excess of 6.25×10^{-3} rad/sec, i.e., the algorithm is exercised each update interval. If no input is received during an update interval, the algorithm does not process and $\dot{Q}_E$ does not exist during that interval. For continuous updating the peak attitude error for a slew input is determined from the figure by the following relationship

$$QE_{\max} = 2\dot{Q}E/W \tag{9}$$

For example, the peak error resulting from the figure with a third-order quaternion algorithm (Honeywell DDP-516 using a 30-bit computer word length) at a 2°/sec system single axis slew rate is 11.3 arc sec.

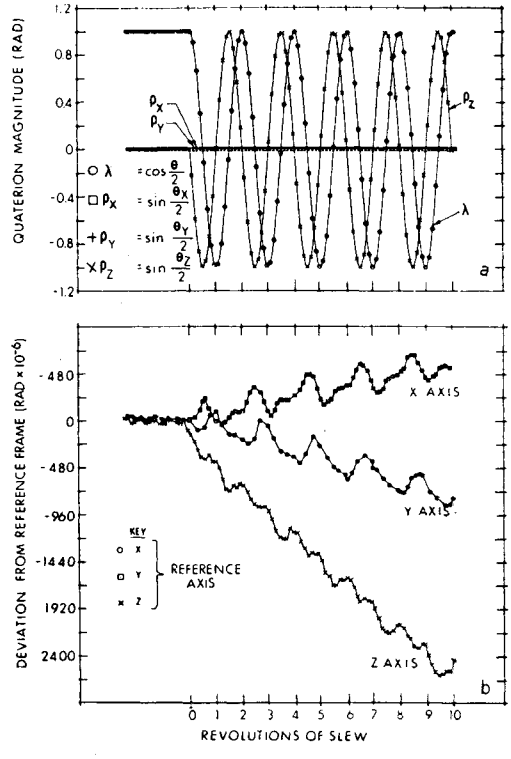

Fig. 14 System test results—slewing input.

End-to-End System Verification

The first- and third-order quaternion algorithms were exercised with the test package and the quaternion attitude output was evaluated by simultaneously recording the table encoder and the four computed quaternion parameters, q_c. A reference quaternion q_p was generated using the table encoder data. System errors were then evaluated by developing a quaternion error q_e that represented the difference between the computed and reference quaternions. The small-angle error representation is

$$\bar{1}_n\theta_e = (q_e - q_e^*) = (q_p^* q_c - q_c^* q_p) \qquad (10)$$

where q^* is the quaternion conjugate. This technique allowed evaluation by generating real-time error profiles for each test sequence.

Earth-rate field tests (Fig. 13) demonstrated gyroscope drift stability and the software mechanization. The system is oriented with respect to the Earth field and the software corrects for instrument biases, Earth rate, etc. Algorithm drift is then plotted versus time. The Z and X axes drift-magnitude offsets represent an error in the corrections used for the instrument drift terms. The 1-meru uncertainty discontinuities appear because gyro data were quantized and the drift and Earth-rate corrections were entered into the algorithm only after integer correction pulse accumulations. This quantization effect masks instrument stability uncertainties, indicating better than 1-meru gyro performance over the 15 hr of operation.

Constant slewing performance of a strapdown system configuration evidences sensitivity to scale factor stability and gyroscope-alignment accuracy. These sensitivities may limit system application for some operational environments.

Figure 14 shows a typical single axis slew-performance test run. A 2°/sec input was applied about the Z axis and a third-order quaternion algorithm was used. This slew run shows a static baseline before initiating 10 revolutions of slew testing. The profile of the four quaternion elements with respect to table slew revolutions is shown in Fig. 14a. As expected, both the λ and ρ_Z parameters track the table rotational angle ($\cos\theta/2$, $\sin\theta/2$) and the ρ_X and ρ_Y attitude does not appear to be changing. The error quaternion propagation for the X, Y, and Z axes is shown in Fig. 14b. The drift rate in X and Y correspond to approximately 5 and 6 meru, respectively. Since these axes are orthogonal to the slew axis, this drift is due to uncorrected gyro-misalignment uncertainties (approximately 3 arc sec). The Z axis data show an error of 2.4 mrad of attitude over the 10 slew revolutions (equivalent to an 18-meru drift rate), corresponding to a SF-correction uncertainty effect of 36 ppm. Recall from Fig. 9 that algorithm slew errors are less than 0.01 meru for the 100 update per second rate. The sinusoidal effect exhibited on all axes corresponds to the computational roundoff error-propagation characteristic discussed previously and the maximum attitude-error amplitude (using 30 bits) agrees closely with the error predicted in the roundoff discussion.

Within the linearity and stability of the gyro and torque loops (50–100 ppm) and the alignment stability of the gyro mounting hardware used, similar results were exhibited over the entire dynamic slew range. These results allow one to project relative performance based on a vehicle's total attitude-maneuver profile.

Single axis oscillatory testing was performed over a frequency range of from 0.5 to 2 Hz and an amplitude from 0.5° to 5° peak-to-peak. (This range of values is compatible with the test table capabilities and the maximum instantaneous torque-to-balance-loop rate capability.) An understanding of the gyro placement with respect to the test package reference axes (Fig. 5) provides a better appreciation of the oscillatory test results. Each gyro OA is coincident with another gyro's IA. Thus, a single axis sinusoidal input is sensed directly by one gyro IA. Because of output axis coupling (Eq. 1), a second gyro also indicates an oscillatory output. Since the output axis coupling signal (W_{OAD}) is proportional to the derivative of the oscillatory motion about its OA, it is 90° phase-displaced from the sensed oscillation on the input axes of the other gyro, i.e.,

$$W_{OAD} = (I_{OA}/H)\dot{W}_{IN} = (I_{OA}/H)(\hat{W}\omega\cos\omega t) \qquad (11)$$

The input oscillation is defined as:

$$W_{IN} = \hat{W}\sin\omega t \qquad (12)$$

$\hat{W}$ is the peak input rate and ω is the sinusoidal frequency.

Thus, for a sinusoidal input, the system algorithm is excited by a sensed gyro IA signal and a gyro OA error. This phenomenon, terms pseudo-coning, is similar to the classical coning model previously described. However, in this case the algorithm operates on an error signal that it assumes is valid and thus corrects for a nonexistent kinematic drift on a third axis. The resulting effect is to generate an algorithm attitude drift error

$$AB\omega/2 = Q \text{ pseudo-coning drift} \qquad (13)$$

where A = peak amplitude of the input displacement along the Y axis, B = peak amplitude of the output-axis displacement along the Z axis, and ω = oscillatory rate = rad/sec. This effect is illustrated by the test run in Fig. 15. A third-order quaternion expansion was used. A 2.3° peak-to-peak, 0.5-Hz single axis oscillatory input was applied about the Y axis of the system. The table motion is shown in Fig. 15a. Notice a small table-drift rate is introduced due to the nonsymmetry of the table friction levels. The table-drift represents a low-level slew, and error effects due to it are negligible. The Y-gyro following error is shown in Fig. 15c. It has a zero-to-peak amplitude of 250 × 10^{-6} radian. Figure 15d shows the induced Z axis gyro OA-coupling signal as approximately 90° phase-displaced from the input oscillation shown in Fig. 15a. Its magnitude is approximately 115 × 10^{-6} rad. The pseudo-coning drift rate about X,

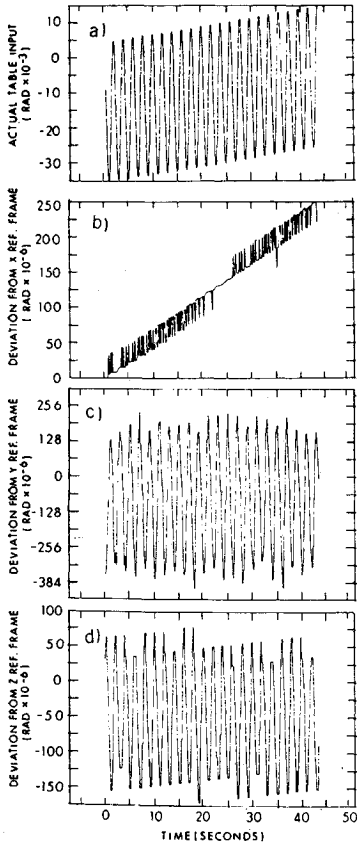

Fig. 15 System test results — oscillatory input.

calculated using the 1.15°, 0.5-Hz input and the OA coupling magnitude, would be 49 meru [Eq. (13)]. Had we calculated the drift theoretically, using the equation for OA coupling [Eq. (1)] and the 18 IRIG nominal parameters, an X axis drift of 41 meru would have been predicted.

The actual measured drift from Fig. 15b corresponds to 56 meru. The difference between the calculated drift from Fig. 15a and d and the actual value of Fig. 15b may be explained in part by uncertainty in the calibration of the X-gyro drift parameters used for correction during this test. Although the test input (in this illustration) represents a severe dynamic environment, inertial-grade performance would have been obtained had OA coupling compensation been used.

Conclusions

This paper has reviewed a wide range of strapdown inertial-system attitude-indication tradeoffs. It has shown that computational whole number attitude-transformation algorithms and inertial-parameter correction algorithms are realizable with current computational equipment. Furthermore, they can be mechanized to operate at moderate update rates and word lengths with negligible system performance degradation. The dynamic-error effects peculiar to the single-degree-of-freedom gyro application in the strapdown torque-to-balance mechanization appear to be predictable and compensatable in the computational algorithms.

Ultimate performance rests with the linearity and stability of the combined gyro and torque-to-balance control loop and the instrument alignment stability. When considering current state-of-the-art design bounds of alignment and SF stabilities, it is interesting to note that their error propagation sensitivities are quite similar. However, alignment effects in a random attitude maneuver environment tend to be self-cancelling.

With regard to these limitations the applicability of an inertial-grade strapdown mechanization is dependent upon the total angle and maneuver profile environment of unaided guidance or navigation phases. Our test findings demonstrate that for a relatively quiescent environment, similar to most current spacecraft and transport aircraft applications, performance over long periods is comparable to basic gyro servo loop or gimbal platform mechanizations. However, one would not consider a strapdown mechanization applied to a constantly rotating spacecraft, a vehicle in which many large angular maneuvers occur early in the unaided mission, or a vehicle in which moderate frequency and amplitude limit cycle oscillations exist for prolonged periods.

References

[1] Turley, A. R., "A Comparison of Three No-Gimbal Inertial Systems by Flight Test on an IBM 7094 Computer," AFAL-tr-65-201, Dec. 1965, Air Force Avionics Lab.

[2] "Initial Results from Road Testing the H-419 (Honeywell) Strapdown Inertial Navigation System," Sept. 1969, prepared by Lockheed Electronics Co. for the Technology Development Branch at NASA/MSC.

[3] "Inertial Subsystems Group, Control, Guidance, and Navigation for Advanced Manned Missions," R-600, Sept. 1968, Vol. IV, Instrumentation Lab., Massachusetts Institute of Technology.

[4] Aronson, J. H. et al., "18 IRIG MOD B Final Report," FBM/IC 021, Dec. 1965–Aug. 1968, Massachusetts Institute of Technology Instrumentation Lab.

[5] Gilmore, J. P. and Feldman, J., "The Gyroscope in Torque-to-Balance Strapdown Application," E-2392, April 1969, Massachusetts Institute of Technology Instrumentation Lab.

[6] McKern, R. A., "A Study of Transformation Algorithms For Use in a Digital Computer," T-493, Jan. 1968, Massachusetts Institute of Technology Instrumentation Lab.